Strain effects in topological insulators: Topological order and the emergence of switchable topological interface states in Sb_2Te_3/Bi_2Te_3 heterojunctions

H. Aramberri and M. C. Muñoz
Instituto de Ciencia de Materiales de Madrid, ICMM-CSIC, Cantoblanco, 28049 Madrid, Spain
(Received 5 December 2016; published 17 May 2017)

We investigate the effects of strain on the topological order of the Bi_2Se_3 family of topological insulators by *ab initio* first-principles methods. Strain can induce a topological phase transition and we present the phase diagram for the 3D topological insulators, Bi_2Te_3, Sb_2Te_3, Bi_2Se_3, and Sb_2Se_3, under combined uniaxial and biaxial strain. Their phase diagram is universal and shows metallic and insulating phases, both topologically trivial and nontrivial. In particular, uniaxial tension can drive the four compounds into a topologically trivial insulating phase. We propose a Sb_2Te_3/Bi_2Te_3 heterojunction in which a strain-induced topological interface state arises in the common gap of this normal insulator–topological insulator heterojunction. Unexpectedly, the interface state is confined in the topologically trivial subsystem and is physically protected from ambient impurities. It can be switched on or off by means of uniaxial strain and therefore Sb_2Te_3/Bi_2Te_3 heterojunctions provide a topological system which hosts tunable robust helical interface states with promising spintronic applications.

DOI: 10.1103/PhysRevB.95.205422

I. INTRODUCTION AND MOTIVATION

Topological insulators (TIs) are a novel quantum phase of matter characterized by a topological invariant [1–3] that exhibit topologically protected states at the boundary with a trivial insulator [4]. In particular, the Bi_2Se_3 family of three-dimensional (3D) TIs has been extensively studied during the past few years as paradigmatic TIs that show an inverted band gap due to a strong spin-orbit coupling (SOC) [5]. At the surface, these materials exhibit a Dirac cone–like helical state with a circular skyrmionic spin texture [6], and the topological protection ensures the robustness of these states against disorder scattering as long as time-reversal symmetry is maintained.

Fundamental interest and potential applications have driven the search of external and internal agents such as stress, electromagnetic fields, chemical substitution, or stacking defects [7], to engineer and manipulate the band structure of TIs. In particular, strain can be exploited to control the topological order. Several works have already assessed the importance of purely uniaxial strain in these materials and its influence on their topological character [8–14]. For bulk materials, it was predicted that the topological phase can be effectively manipulated by strain [9]. Uniaxial strain can be induced by the chemical intercalation of zerovalent nonmagnetic metals in the van der Waals (vdW) gaps. This technique has already been experimentally demonstrated and developed by Koski *et al.* [15] in Bi_2Se_3 to effectively enhance the c lattice parameter without disrupting the ionic or electronic configuration. In addition, Bi_2Se_3 films under tensile stress along the c axis have been recently grown via a self-organized order method and significant changes of the Fermi level and band gap of those films have been measured [16]. Topological state shifts at the strained grain boundaries in Bi_2Se_3 films have also been reported [8]. To our knowledge, no study has systematically addressed the combined effect of both uniaxial and biaxial strain in the topology of the Bi_2Se_3 family. Being the four compounds narrow gap semiconductors, small strain fields can strongly affect their electronic properties, and, consequently, their topological nature. In this work we study the role of combined uniaxial and biaxial tension on the Bi_2Se_3 family of compounds, namely Bi_2Te_3, Sb_2Te_3, Bi_2Se_3, and Sb_2Se_3.

We show how uniaxial and biaxial strain can tune several properties of the topological states and how the combined effect of both kinds of strain can drive the four systems into a metallic phase or two topologically distinct insulating phases. We calculate the phase diagram for the four materials in terms of uniaxial and biaxial strain, and we show the band inversion process that governs their topology. Furthermore, we predict the emergence of strain induced topological interface states in Sb_2Te_3/Bi_2Te_3 heterojunctions. The article is structured as follows: in Sec. II we describe the methods employed for the calculations along with the crystal structure of the Bi_2Se_3 family of compounds. Section III is devoted to the effect of uniaxial and biaxial strain in bulk and thin films of the studied compounds. Next, we propose two topologically distinct heterojunctions of Bi_2Te_3 and Sb_2Te_3 and address their special electronic properties in Sec. IV. Finally, Sec. V includes a summary of the results and conclusions.

II. METHODS AND CRYSTAL STRUCTURE

Bismuth dichalcogenides show a rhombohedral crystal structure with a five atom basis that constitute a quintuple layer (QL)—see Fig. 1. The four compounds forming the Bi_2Se_3 family studied in this work belong to the $R\bar{3}m$ (D^5_{3d}) crystallographic group. Along the [111] direction each atomic layer contains only one element and is hexagonally compact. The stacking pattern along this direction is ...AbCaB..., where capital (small) letters indicate the position of Se or Te (Bi or Sb) atoms. Within a QL, interactions among the atoms are strong, while inter-QL bonding is of the weaker vdW kind.

To model the systems we employed the Vienna *ab initio* simulation package (VASP) [17] density functional theory (DFT) code for the atomic relaxations and electronic structure calculations of bulk materials. The SIESTA code [18], through its implementation in the GREEN package [19], was additionally used for electronic structure calculations of the Bi_2Te_3–Sb_2Te_3 heterojunctions. In all the calculations we used

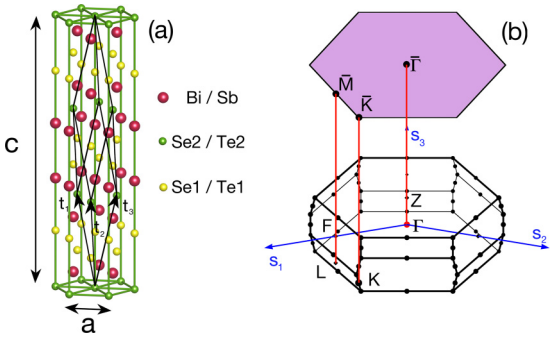

FIG. 1. (a) Rhombohedral unit cell of the four studied compounds. Lattice constants a and c are indicated in the figure. (b) The corresponding bulk Brillouin zone along with its projection along the [111] direction (purple shaded area).

the Perdew-Burke-Ernzerhof [20] implementation of the generalized gradient approximation (GGA). The semiempirical pair-potential vdW correction of Grimme [21] was used in the atomic relaxations as implemented in the VASP code to correctly account for the weak inter-QL interaction. The spin-orbit coupling was included self-consistently in both VASP [22] and SIESTA-GREEN [23] calculations. A 340 eV energy cutoff was employed for the plane wave basis set in VASP calculations, while a double ζ-polarized scheme with confinement energies of 100 meV was used for the numerical atomic orbital basis set in SIESTA. Three-center integrals in SIESTA were computed using a hyperfine mesh cutoff of 1200 Ry, equivalent to a real space grid resolution below 0.05 Å^3. Biaxial (uniaxial) strain was taken into account by elongating or contracting lattice parameter a (c)—see Fig. 1—and allowing the internal coordinates of the ions to relax. Biaxial and uniaxial strain (ϵ_a and ϵ_c, respectively) of a particular compound with lattice parameters a,c are given by

$$\epsilon_a = (a - a_{eq})/a_{eq},$$
$$\epsilon_c = (c - c_{eq})/c_{eq}, \quad (1)$$

where a_{eq} and c_{eq} are the equilibrium values of the in-plane and out-of-plane lattice parameters, respectively.

III. UNIAXIAL AND BIAXIAL TENSION

A. Bulk materials

To address the effects of biaxial tension, we first calculated the total energy of the Bi_2Se_3 family of compounds for different values of the lattice constants using GGA+vdW with the VASP code. In this way, we obtain the relaxed geometry for a fixed value of the in-plane lattice parameter a. Figure 2 shows the total energy of Bi_2Te_3, Sb_2Te_3, Bi_2Se_3, and Sb_2Se_3 for different values of a as a function of the out-of-plane lattice constant c. The equilibrium lattice parameters a_{eq} and c_{eq} were also calculated, and are given in Table I. In Fig. 3 we show the band structure of fully relaxed Bi_2Se_3 for both bulk and thin film geometries as a reference. As shown in Fig. 2, for compressive in-plane biaxial strains ($\epsilon_a < 0$) lattice parameter c tends to increase, while for tensile strains ($\epsilon_a > 0$) c decreases with respect to its equilibrium value. In fact, we can estimate the value of the Poisson ratio ν from our calculations with the following equation for equibiaxial strained

TABLE I. Calculated values of the equilibrium lattice parameters of the Bi_2Se_3 family of compounds. Relaxations were carried out with VASP in the GGA+vdW approximation. Values in parentheses correspond to experimental data from Ref. [25]. No experimental data was available for Sb_2Se_3 in the rhombohedral phase.

	Bi_2Te_3	Sb_2Te_3	Bi_2Se_3	Sb_2Se_3
a_{eq} (Å)	4.40 (4.383)	4.25 (4.25)	4.17 (4.138)	4.04 (–)
c_{eq} (Å)	30.5 (30.487)	30.9 (30.35)	28.4 (28.64)	28.7 (–)

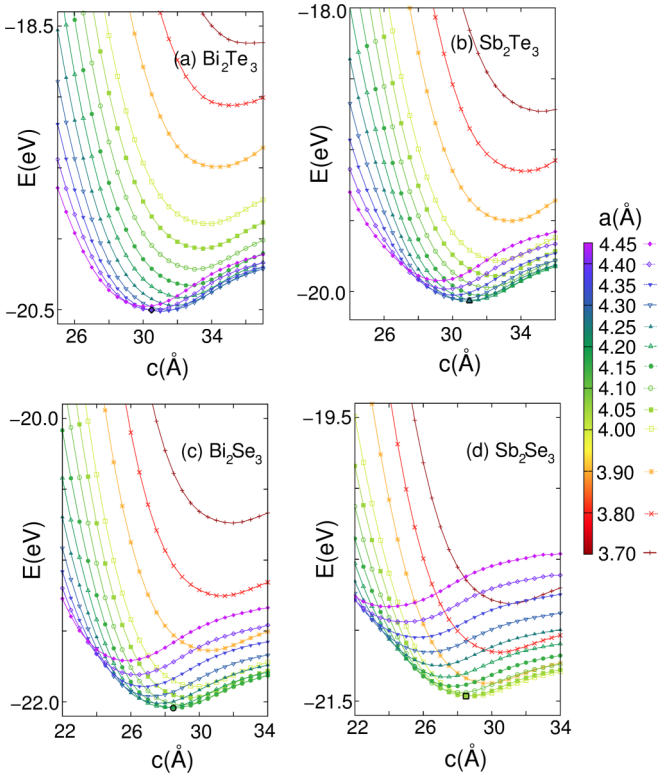

FIG. 2. Total energy calculations using GGA+vdW in VASP for (a) Bi_2Te_3, (b) Sb_2Te_3, (c) Bi_2Se_3, and (d) Sb_2Se_3. Each curve shows the energy versus c for a fixed value of a (see legend at the right). Symbols marked in black indicate the equilibrium configuration. The exact values of the equilibrium lattice parameters are given in Table I.

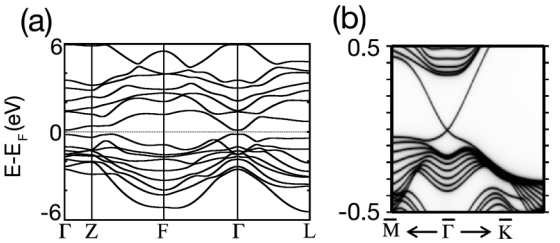

FIG. 3. (a) Bulk band structure of fully relaxed Bi_2Se_3. The system is insulating and shows an inverted band gap. (b) Band dispersion of a 6 QL Bi_2Se_3 slab. Topological surface states with a Dirac-like dispersion expand the bulk band gap, evidencing the topological character of unstrained Bi_2Se_3.

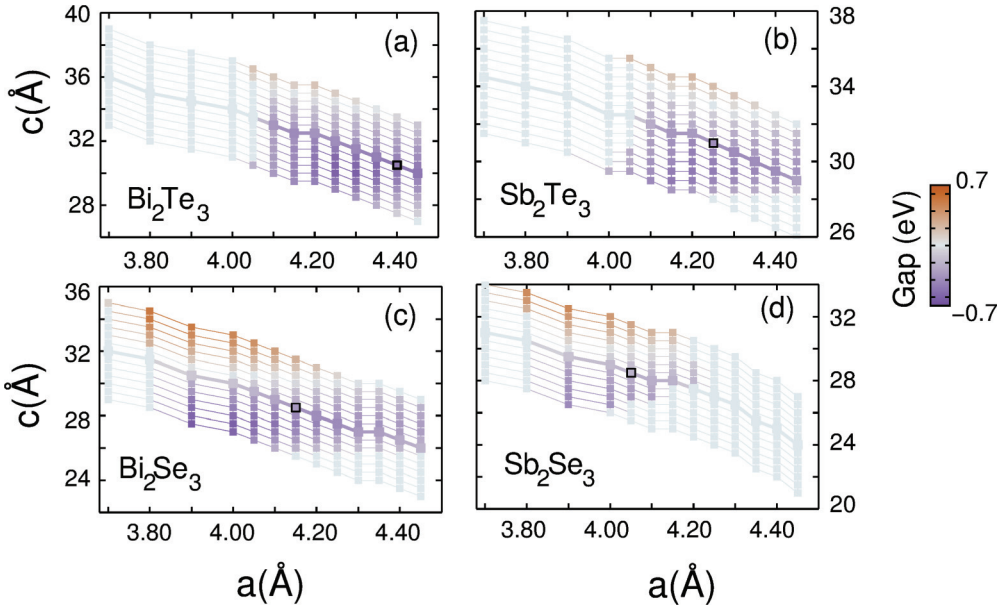

FIG. 4. (a) Band gap (in color code shown on the right) for Bi_2Te_3 for different values of lattice constants a and c. The ionic configurations were allowed to relax for every single calculation. Negative gaps (purple) indicate that the energy of Bi p_z orbital is lower than the Se p_z orbital, i.e., the system is topologically nontrivial. Panels (b), (c), and (d) show equivalent diagrams for Sb_2Te_3, Bi_2Se_3, and Sb_2Se_3 respectively. These phase diagrams show the regions in phase space where the system is a normal insulator (orange), a TI (purple), or a metal (gray). The equilibrium position is marked with a black square and the thicker line corresponds to the relaxed c lattice parameter for a fixed value of a for each system.

systems [24]:

$$\epsilon_c = -\frac{2\nu}{1-\nu}\epsilon_a. \tag{2}$$

Fitting the energy minima positions for the curves shown in Fig. 2 to Eq. (2) we obtain Poisson ratios of 0.30, 0.32, 0.29, and 0.27 for Bi_2Te_3, Sb_2Te_3, Bi_2Se_3, and Sb_2Se_3, respectively, in agreement with previous calculations [13,26,27].

In order to address the combined effects of out-of-plane uniaxial and in-plane biaxial strain, the phase diagram of the Bi_2Se_3 family of compounds was computed for several points in parameter space (a,c). For every pair of values of the lattice constants, we allowed the ionic positions to relax and we calculated the energy spectrum. In this way we can address the combined effect of uniaxial (along the c direction) and biaxial strain. The results are summarized in Fig. 4 for the four compounds. For a fixed value of a, points along vertical lines correspond to increments of ∼1.5% of uniaxial strain, the central point of each vertical line being the relaxed value of c for the given amount of biaxial strain in that line. For the four systems, three distinct phases can be identified: a metallic phase, a topologically trivial insulating phase—normal insulator (NI), with $\mathbb{Z}_2$ topological invariant 0—and a topologically nontrivial phase—topological insulator (TI), with $\mathbb{Z}_2$ topological invariant 1—. The metallic phase is obtained for large in-plane biaxial strains in any direction. This is due to the fact that a high compressive in-plane strain enhances the bandwidth of the p_x and p_y orbitals in the valence band (VB), which eventually crosses the Fermi level and makes the system metallic. For high tensile in-plane biaxial strains, the conduction band (CB) undergoes an analogous process, leading also to a metallic system. For moderate in-plane strains (below ∼10% in absolute value) the systems remain insulating. In this range, the topological behavior of these systems is governed by the band inversion between the Se and Bi p_z bands, and a topological phase transition (TPT) can be induced by out-of-plane strain. Starting from an inverted phase, for $\epsilon_c < 0$ the bandwidth of the p_z bands is enhanced, which in turn makes the gap bigger at first, until eventually the gap becomes indirect, starts to decrease, and at a certain large compressive out-of-plane strain the system becomes metallic again. On the other hand, tensile out-of-plane strain ($\epsilon_c > 0$) tends to diminish the gap until it closes when the energies of the Bi and Se p_z bands at the $\bar{\Gamma}$ point become equal. Further tensile strain reopens the gap, turning the system into a topologically trivial insulator. Figure 5 shows the behavior of the gap with out-of-plane strain for Bi_2Se_3 at $a = 4.20$ Å. The band gap closing and reopening is evident from the crossing between the Bi and Se p_z bands, which have opposite parity and are responsible for the topological nature of the Bi_2Se_3 family of compounds [5].

For $\epsilon_a = 0$, the critical uniaxial strain driving the TPT for Sb_2Se_3, Bi_2Se_3, Sb_2Te_3, and Bi_2Te_3 is 3%, 6%, 6%, and 12%, respectively. This trend is in turn related to the crystal structure *and* the strength of the SOC in each system, being largest in Bi_2Te_3, smallest in Sb_2Se_3, and intermediate in Bi_2Se_3 and Sb_2Te_3. Note that this values are given for zero biaxial in-plane strain, and the TPT will occur at different values of ϵ_c for $\epsilon_a \neq 0$ (see Fig. 4). Other studies have shown similar TPTs for Bi_2Se_3-like systems under purely uniaxial strain of 6%–10% [8–14], which is in good agreement with our results.

Recent studies have revealed the importance of quasiparticle corrections [28,29] and temperature effects [30], which lead to a renormalization of the single-particle bands. However, according to those studies the band inversion persists and the

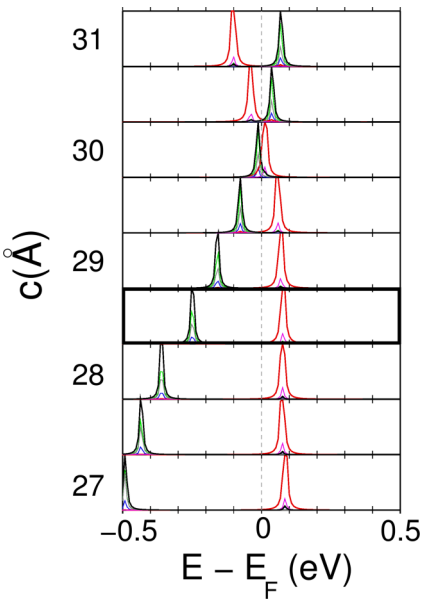

FIG. 5. Projected density of states (PDOS) in the Γ point around the energy gap for bulk Bi_2Se_3 with lattice parameter a fixed to 4.20 Å and different values of c (left axis). The equilibrium configuration is marked with a thicker frame. Black and red lines show the contribution of Bi p_z and Se p_z orbitals, respectively. The magenta and blue lines indicate the Bi and Se s contributions, while the gray and green lines depict the Bi and Se $p_x + p_y$ weight. At $c \sim 30$ Å the bulk band gap closes and the system undergoes a topological phase transition, so that for $c > (<)$ 30 Å the bands are *uninverted* (inverted) and the system is topologically trivial (nontrivial). The different behavior of the Se and Bi p_z bands with uniaxial strain is apparent in the figure.

value of the $\mathbb{Z}_2$ invariant remains unchanged. Therefore, the inclusion of both effects could slightly modify the values of the critical strains, but our results should remain qualitatively correct. In fact, although DFT is known to underestimate band gaps, we find very good agreement between our computed band gaps and experimental data [25,31].

The universal phase diagram for the Bi_2Se_3 family of 3D TIs under the combined effect of uniaxial and biaxial strain is sketched in Fig. 6. We systematically address the effects on the topology of combined uniaxial and biaxial strain. Moreover, as the four systems show a positive Poisson ratio, pure compressive biaxial strain induces an expansion in the c

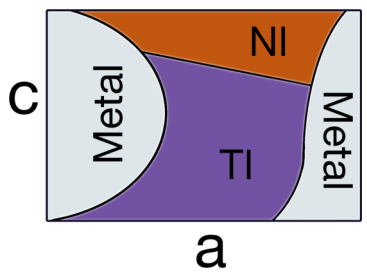

FIG. 6. Schematic universal phase diagram for Bi_2Se_3-like systems in (a,c) parameter space. For high tensile and compressive in-plane strain the system becomes metallic. Uniaxial strain applied in the out-of-plane direction triggers a TPT.

direction which could, in principle, drive the system into the normal insulating phase. Nevertheless, if no additional uniaxial strain is applied, we find that the four systems undergo a TI to metallic phase transition with both tensile and compressive biaxial strain. The phase diagram we provide for the four compounds can be useful for topological, band, and orbital engineering of the Bi_2Se_3 family of compounds in the fields of straintronics and spintronics.

The Sb_2Se_3 compound

Our results predict unstrained Sb_2Se_3 to be a topologically nontrivial insulator in the $R\bar{3}m$ phase. Nevertheless, the region of parameter space in which Sb_2Se_3 is a TI is small and therefore minor variations of the lattice parameters result in a trivial insulator. Previous calculations have reported this material to be a normal insulator [5,13,32] under no strain. Comparing with Refs. [5,32], we obtain slightly smaller lattice constants ($a = 4.04$ versus 4.076 Å, $c = 28.7$ versus 29.83 Å for Ref. [5], and similar values for Ref. [32]), probably due to the inclusion of vdW corrections in our calculations. With their lattice constants our calculations also predict Sb_2Se_3 to be a narrow gap NI—see Fig. 4(d). In Ref. [13] they obtain lattice parameters closer to ours ($a = 4.026$ Å, $c = 28.732$ Å) within the GGA+vdW approximation, but decide to set the equilibrium (unstrained) configuration at the plain GGA relaxed parameters (without the vdW correction, $a = 4.078$ Å, $c = 29.92$ Å), yielding again a NI phase. Recent calculations by another group [33] estimate smaller values of lattice parameters for rhombohedral Sb_2Se_3 ($a = 4.004$ Å, $c = 28.553$ Å) and seem to predict an inverted band structure for antimony selenide—see the curvature of the bands around the Γ point in Fig. 2(d) of Ref. [33], but do not elaborate on its topological nature. Unfortunately, experimental data for Sb_2Se_3 is only available for its more stable orthorhombic phase (*Pnma*) [34]. We recently became aware of another work [35] in which DFT+vdW calculations predict rhombohedral Sb_2Se_3 to be topologically nontrivial.

B. Thin films

Now we investigate the effect of pure biaxial in-plane strain along with low dimensional effects on thin films of Bi_2Se_3-like systems. Our starting points are bulk calculations in which, for a fixed amount of biaxial strain, the lattice parameter c was allowed to fully relax along with the atomic coordinates. These bulks correspond to the equilibrium systems for each value of the in-plane strain and coincide with the minimum of each curve for fixed a in Fig 2, and with the thick lines in Fig. 4. Then, slabs of 1, 2, 3, 4, and 6 QL thicknesses were built with the bulk positions and their band dispersions were computed. The results for Bi_2Se_3 are shown in Fig. 7 for the range of lattice parameter a in which the bulk system is a TI (see the results for Bi_2Te_3, Sb_2Te_3, and Sb_2Se_3 in the Appendix, for the same range of lattice parameters).

The behavior with both compressive and tensile biaxial strain of Bi_2Se_3 thin films is in clear analogy with the bulk behavior. Nevertheless, they show distinct features induced by strain. Under compressive biaxial strain the size of the Bi_2Se_3 bulk gap acquires a smaller value than that of the unstrained system, and therefore the penetration depth of the surface

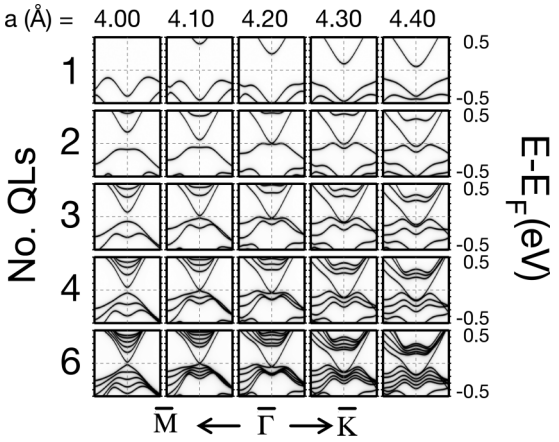

FIG. 7. Band dispersion diagrams close to the $\bar{\Gamma}$ point along the $\bar{M}-\bar{\Gamma}-\bar{K}$ directions for Bi_2Se_3 slabs under biaxial strain. Each column corresponds to a fixed value of the in-plane lattice parameter labeled on top and the corresponding out-of-plane c parameter. The calculated equilibrium in-plane lattice parameter of unstrained Bi_2Se_3 bulk is 4.17 Å . The five rows correspond to different slab thicknesses: 1, 2, 3, 4, and 6 QLs from top to bottom. The horizontal dashed lines indicate the Fermi level, whereas the vertical dashed lines show the $\bar{\Gamma}$ point.

states is enlarged and a larger number of layers is needed to close the hybridization gap. Moreover, the "M"-shaped feature in the VB around the $\bar{\Gamma}$ point is smoothed out and consequently the linear dispersion of the TSS is extended to a larger energy region in the VB. On the other hand, applying tensile biaxial strain also tends to close the bulk gap, but the M-shaped feature becomes more pronounced and hence the DP in the films is shifted inside the VB (see the 6 QL series in Fig. 7). A sharp enough M-shaped VB detaches the DP from the Fermi level and consequently induces an n-type doping of the surface states. This result explains the shift in the DP observed in Ref. [14], as well as the different behavior, gap opening or n doping, observed at the grain boundaries in Bi_2Se_3 films, in regions under compressive or tensile strain, respectively [8].

Moreover, a small decrease in the Fermi velocity with tensile strain is also apparent. The penetration depth of the TSS also varies with strain, and the closer in the phase diagram to the critical metal-TI lines the more QLs are needed to close the hybridization gap (see, for instance, the 2 QL series in Fig. 7, in which compressive or tensile biaxial strain takes the system closer to a critical line in the phase diagram, and the TSS are gapped but for $a = 4.20 \approx a_{eq}$), in agreement with the results displayed in Ref. [8]. Higher compressive biaxial strain drives the thin films into a metallic state due to the upward shift in energy of the valence band maximum (see, for example, Fig. 16 in the Appendix), while for a critical tensile biaxial strain the bulklike CB crosses the Fermi level and the thin films become metallic again (see Fig. 18).

Strain can therefore turn the Bi_2Se_3 family of compounds insulating or metallic, and allows for engineering of the gap, the orbital character of the bands, the Fermi velocity, DP energy, and thus also the doping of the TSSs. The tablelike figures for the four systems are displayed so that they can be used for determining what kind of band dispersion is expected when a bismuth dichalcogenide of a certain thickness is grown on a substrate with a particular lattice parameter.

TABLE II. Electronegativities of the four elements present in the Bi_2Se_3 family of compounds according to the Pauling scale (first row) and the Allen scale (second row). Bi and Sb present very similar values, whereas the difference between the electronegativities of Te and Se is significant in both scales.

	Bi	Sb	Te	Se
χ_P [36]	2.02	2.05	2.1	2.55
χ_A [37]	2.01	1.984	2.158	2.434

IV. STRAINED HETEROJUNCTIONS

When two distinct TIs are faced to one another, an interesting problem arises. If both materials belong to the same $\mathbb{Z}_2$ topological class, no interface state is guaranteed by the bulk-to-boundary correspondence, as the change in topological invariant is zero. Therefore, a topological surface state can be annihilated by placing another TI on top, even if both bulk gaps align in a straddling gap configuration. Still, topologically trivial interface states may arise regardless of the topological invariants. Moreover, in broken gap heterojunctions (without a common gap) no topologically protected interface state may appear since the system will no longer be an insulator. In this section we will study interfaces of Bi_2Te_3 and Sb_2Te_3 both in superlattices and in slab geometry. Among the four members of the Bi_2Se_3 family of compounds, we have chosen these two so that the difference in electronegativity, χ, between the A and B elements in the A_2B_3 compounds is as small as possible, in order to obtain a straddling gap at the heterojunction and minimize the band bending along the system. Table II shows the Pauling and Allen electronegativities (χ_P and χ_A) for Bi, Sb, Te, and Se. The first two elements have an almost equal value of the electronegativity—in fact $\chi_P(\mathrm{Bi}) < \chi_P(\mathrm{Sb})$, while $\chi_A(\mathrm{Bi}) > \chi_A(\mathrm{Sb})$. On the other hand, Se and Te show a bigger difference in their χ values. Opposite doping for Se- and Te-based materials is expected, and we have additionally calculated Bi_2Se_3/Bi_2Te_3 heterojunctions which exhibit a broken gap alignment, thus leading to a metallic phase where the $\mathbb{Z}_2$ invariant is ill defined and no topological interface states can exist.

A. TI/TI interfaces

We have chosen $Sb_2Te_3/Bi_2Te_3/Sb_2Te_3$ trilayers with equal number of QLs of Sb_2Te_3 at both sides so that inversion symmetry is preserved, making the analysis simpler, as both interfaces will be equivalent. We calculated $m-Sb_2Te_3/n-Bi_2Te_3/m-Sb_2Te_3$ trilayers, where m and n are the number of QLs of Sb_2Te_3 and Bi_2Te_3, respectively. In the superlattice geometry, due to periodic boundary conditions, the trilayer turns into a $2m-Sb_2Te_3/n-Bi_2Te_3$ structure repeated in the [111] direction. We still call it a $m-Sb_2Te_3/n-Bi_2Te_3/m-Sb_2Te_3$ superlattice to emphasize the centrosymmetric nature of the system. We fixed $n = 6$, for which the surface-surface interaction in Bi_2Te_3 is negligible and a gapless Dirac cone (DC) develops at the surface—see

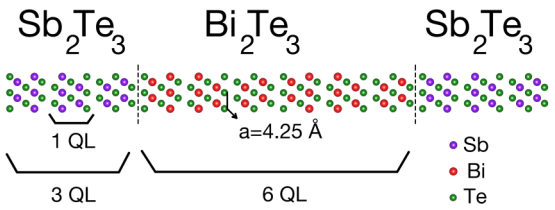

FIG. 8. Geometry of the $m-Sb_2Te_3/n-Bi_2Te_3/m-Sb_2Te_3$ trilayer with $m = 3$ and $n = 6$. The in-plane lattice parameter a is fixed to that of Sb_2Te_3 under no strain. Interfaces are shown as dashed lines as a guide to the eye. The whole system follows the AbCaB stacking pattern analogous to an fcc (111) crystal, which ensures inversion symmetry is preserved. Superlattices are constructed by imposing periodic boundary conditions on this and similar trilayers, which will also preserve inversion symmetry.

Fig. 9(a), while the number of Sb_2Te_3 QLs at both sides is varied from $m = 1$ to 3. The AbCaB stacking sequence of the pristine subsystems is preserved along the interfaces and in the superlattices in order to preserve inversion symmetry. The C_3 rotation axis and the three vertical mirror planes of the pristine systems are also preserved in the heterojunction. We fix the in-plane lattice vector a to that of Sb_2Te_3 in equilibrium, $a_{eq} = 4.25$ Å, and the c lattice parameter for each subsystem is set to its relaxed value for a fixed to the aforementioned value, that is 30.9 Å for Sb_2Te_3 and 32.0 Å for Bi_2Te_3 (see Fig. 2). The ionic coordinates within each subsystem are fixed to their relaxed bulk values, and the vdW gap between Sb_2Te_3 and Bi_2Te_3 is taken as the average vdW gap between both subsystems. This setup could correspond to a 6 QL thick Bi_2Te_3 slab grown on a m-QL Sb_2Te_3 substrate, and another m-QL Sb_2Te_3 thin film grown on top of it. Figure 8 depicts the geometry for the $m = 3$ case. According to the phase diagram calculated in Fig. 4, both the Sb_2Te_3 and Bi_2Te_3 subsystems show an inverted gap in the bulk. This means that the existence of an interface state is not guaranteed, since the change in the $\mathbb{Z}_2$ invariant across the interface is zero as both materials are topological insulators.

We start by analyzing the electronic structure of the isolated subsystems, depicted in Fig. 9. Bi_2Te_3 under small biaxial strain remains a TI, and so it develops surface states when truncated in the [111] direction. For a 6 QL slab (as shown in the figure), surface-surface interaction is already negligible and the linearly dispersive DCs at the $\bar{\Gamma}$ point emerge. In contrast with Bi_2Se_3 or Sb_2Te_3, the DP of the Bi_2Te_3 surfaces is not at the Fermi level and lies below the VB maximum. This is in agreement with previous results [5], and can be attributed to the larger curvature of the VB along the $\bar{\Gamma} - \bar{M}$ direction. Sb_2Te_3 in this system presents neither uniaxial nor biaxial strain, and it is therefore also in the topologically nontrivial phase. In Fig. 9 the electronic structure of unstrained 1, 2, 3, 4, and 6 QL thick Sb_2Te_3 films is also shown—panels (b) to (f). Antimony telluride presents a topological surface state being the DP at the Fermi level for 6 QLs. The penetration depth is ∼2 QLs, so that a gap opens in thin films of less than 5 QLs due to surface-surface hybridization.

The band structures of the periodic superlattices are shown in Figs. 10(a) to 10(c) for $m = 1$, 2, and 3, and those corresponding to the trilayer slabs in Figs. 10(d) to 10(f). The former—(a), (b), and (c)—present a band gap of 0.1 eV, with a VB(CB) offset of 0.1 (0.05) eV between both subsystems, and the VB (CB) of Sb_2Te_3 lying at a higher energy. The small band staggering at the heterojunction can be attributed to the small deviation in the values of the electronegativity for Bi and Sb. Figures 11(a), 11(b), and 11(c) represent the atomic orbital decomposed partial density of states (PDOS) at $\bar{\Gamma}$ in the energy region displayed in Fig. 10. They evidence the band inversion in both Sb_2Te_3 and Bi_2Te_3 slabs and the similar band alignment for the three superlattices, $m = 1$, 2, and 3. The top of the VB is dominated by Sb and Bi p_z orbitals with positive parity, the former being at higher energy, while the Te p_z

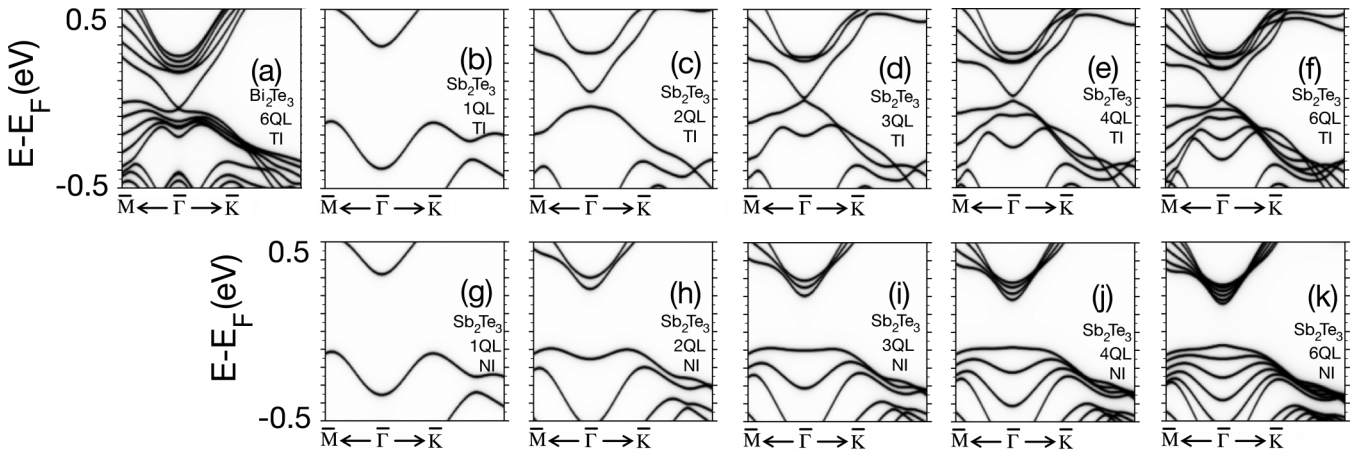

FIG. 9. Band structure of the different isolated subsystems involved in the TI/TI/TI trilayers—top row, (a) to (f)—and in the NI/TI/NI trilayers—bottom row and (a). Panel (a) corresponds to a 6 QL Bi_2Te_3 thin film under biaxial compressive strain so that its in-plane lattice parameter matches that of equilibrium Sb_2Te_3 (4.25 Å). Panels (b) to (f) show the band dispersion for unstrained Sb_2Te_3 slabs of 1, 2, 3, 4, and 6 QLs, respectively, which show a TSS according to their topologically nontrivial nature, although for thicknesses below ∼5 QL a gap opens in the TSSs due to surface-surface interaction. Panels (g) to (k) show the electronic structure of uniaxially elongated Sb_2Te_3 slabs of 1, 2, 3, 4, and 6 QLs, respectively. In these cases the system is clearly in the normal insulating regime, since no TSS appears for thicknesses as large as 6 QL.

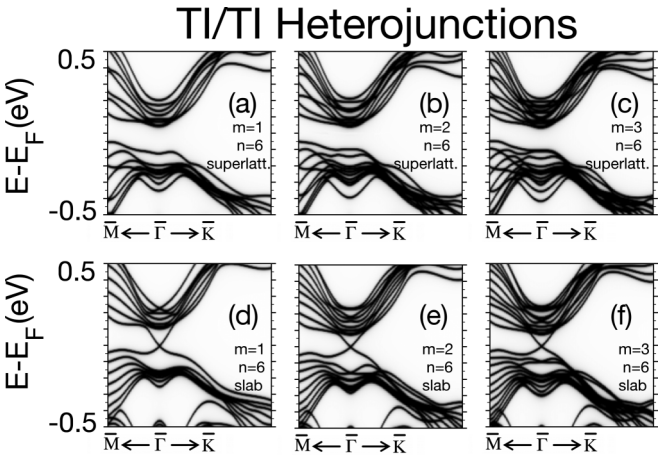

FIG. 10. Band structure of the TI/TI/TI heterojunctions considered, both in superlattice—(a) to (c)—and slab—(d) to (f)—geometries. Panels (a), (b), and (c) show the band dispersion for the trilayers in a superlattice with $n = 6$ and $m = 1, 2$, and 3, respectively. As all the constituents of the superlattice are topologically nontrivial, there are no interfaces between subsystems with different value of the $\mathbb{Z}_2$ topological invariant, and no interface state exists. Panels (d), (e), and (f) correspond to slab geometries with $n = 6$ and $m = 1, 2$, and 3, respectively. In these three cases a surface state develops irrespective of the number of Sb_2Te_3 layers, but no interface state is present.

orbitals with negative parity are located at the bottom of the CB region. The interaction between the CB Te orbitals of both compounds is weak, particularly for the wider superlattices. Hence, in the superlattice, both subsystems present an inverted band structure.

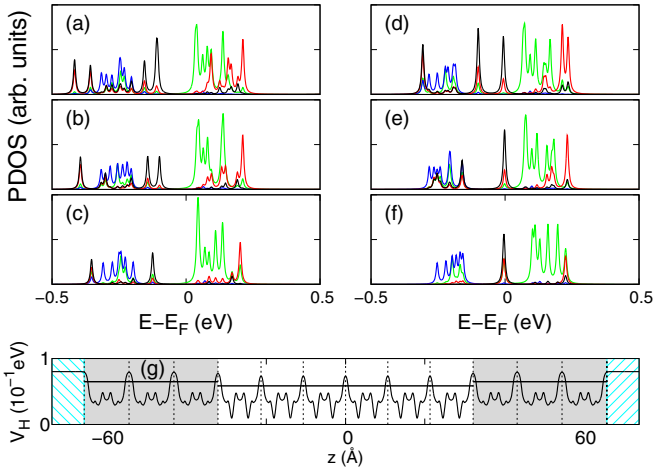

FIG. 11. Panels (a) to (f) show the PDOS in $\bar{\Gamma}$ close to the Fermi level of the studied TI/TI heterojunctions. Blue and black lines show the contribution of Bi p_z and Sb p_z orbitals, respectively. The green and red lines indicate the Te p_z contributions from the Te atoms in the Bi_2Te_3 and Sb_2Te_3 subsystems respectively. Panels (a) to (c)—(d) to (f)—depict the PDOS for superlattices—slabs—with $m = 3$ to 1. Both subsystems show an inverted band structure in all cases. The 2D averaged Hartree potential profile for the $m = 3$ TI/TI slab is shown in (g), along with the average Hartree potential in each QL (horizontal straight solid lines).

The bulk-to-boundary correspondence predicts no topologically protected interface state at the junction, and although trivial interface states could develop, our results show that this is not the case. We therefore conclude that this Sb_2Te_3/Bi_2Te_3 heterojunction is insulating with no interface states whatsoever, but will develop surface states when truncated. This is proved in the thin film geometry—Figs. 10(d), 10(e), and 10(f), where surface states that span the whole bulk band gap appear at both ends. The DP of these TSSs is pinned at the Fermi level irrespective of the thickness of the Sb_2Te_3 layers. In fact, even for the $m = 1$ and 2 for which the thickness of the Sb_2Te_3 subsystem is below the penetration depth of the surface states—see Figs, 9(b) and 9(c)—there is no energy gap and the spectrum of the trilayer slab still exhibits a semimetallic character. The corresponding atomic orbital PDOS are shown in Figs. 11(d) to 11(f). The three trilayers exhibit a sharp peak at $\bar{\Gamma}$, associated with the TSSs. They have a predominant contribution of the Sb_2Te_3 orbitals, mostly of Sb p_z.

This orbital contribution is consistent with the TSS localization shown in Fig. 12(a), for the three different slabs. The surface state is strongly confined in the Sb_2Te_3 subsystem, with a penetration depth of $\approx$2 QLs, although for the $m = 1$ case the state strongly localizes at the surface-most QL. Figure 11(g) displays the 2D averaged Hartree potential profiles—including the ionic contribution—along the [0001] direction for the $m = 3$ slab. It reflects the chemical difference between both Sb_2Te_3 and Bi_2Te_3 compounds and the potentials are almost identical for the finite trilayers and the superlattice (not shown), differing only on the potential step at the surface of the slab. Therefore, our results corroborate the fact that unstrained Sb_2Te_3 is a TI even for ultrathin films, and support the idea that the TI/TI $Sb_2Te_3-Bi_2Te_3$ heterojunction behaves as a homogeneous TI and confines neither topological nor trivial states at the interface.

B. NI/TI interfaces

Now we will discuss the effect of applying uniaxial tensile strain to Sb_2Te_3 in the system presented in the previous subsection. The systems considered are again $m-Sb_2Te_3/n-Bi_2Te_3/m-Sb_2Te_3$ trilayers in either a slab geometry (thin film) or a superlattice. The in-plane lattice parameter is again fixed to $a = 4.25$ Å and c is set to 32.0 Å for Bi_2Te_3, but now the Sb_2Te_3 subsystem is expanded to $c = 34.0$ Å, corresponding to a uniaxial tensile strain of -10%. According to the phase diagram shown in Fig. 4, Sb_2Te_3 will now be in a normal insulating phase, so that at the interface of Sb_2Te_3 and Bi_2Te_3 the topological $\mathbb{Z}_2$ invariant will increase from 0 to 1. The TPT on Sb_2Te_3 can be induced by external uniaxial tensile strain or via the chemical intercalation of zerovalent nonmagnetic metals in the vdW gaps [15] as stated in a previous section.

The electronic structure of the different isolated constituents is shown in Figs. 9(a) and 9(g) to 9(k). Sb_2Te_3 under such out-of-plane strain shows no band inversion in the bulk, and this is reflected in the thin film electronic structure. In contrast with the previously analyzed systems, Sb_2Te_3 now shows no surface state since it is in the NI phase. The gap is of 0.4 eV for the 1 QL slab—Fig. 9(g)—and decreases down to 0.2 eV for the 6 QL thin film—Fig. 9(k). On the

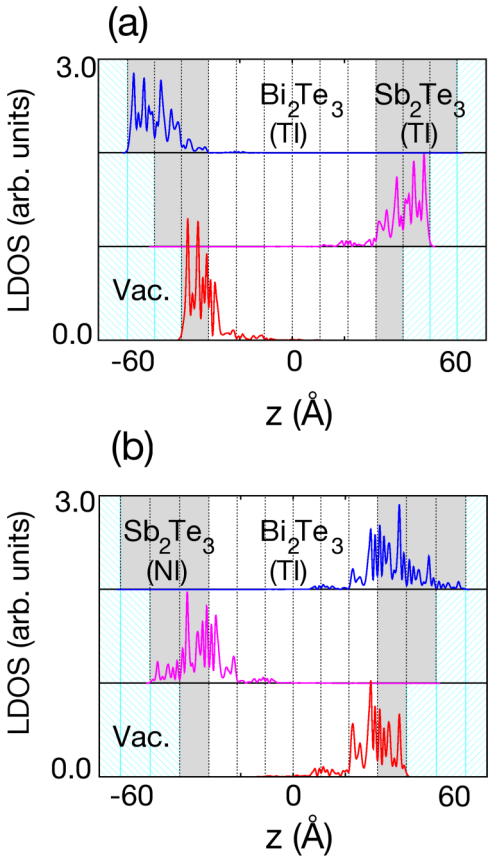

FIG. 12. Layer projected density of states (LDOS) of the topological states in $m-Sb_2Te_3/n-Bi_2Te_3/m-Sb_2Te_3$ trilayer slabs for $m = 1$ (red line at the bottom), $m = 2$ (magenta line in the middle), and $m = 3$ (blue line at the top). The LDOS was computed at $\boldsymbol{k} = (5,0) \times 10^{-3}$ Å^{-1}, along the $\bar{\Gamma} - \bar{K}$ direction and close to the $\bar{\Gamma}$ point for the electronlike TSSs. The trilayer is centered at the middle of the 6 QL Bi_2Te_3 layer. Vertical dashed lines depict the boundaries of each QL. The gray shaded region corresponds to the Sb_2Te_3 subsystem, while white regions belong to the Bi_2Te_3 subsystem and the vacuum is shaded with a cyan pattern. Panel (a) shows the TI/TI/TI trilayer for which TSSs localize at the surface-most QL of the Sb_2Te_3 which is in the topological insulating phase. In (b) the LDOS of the NI/TI/NI trilayer is shown. In this case TISs localize at both interfacial QLs, one in the Bi_2Te_3 subsystem and the other in the Sb_2Te_3 subsystem, with the latter being in the NI phase. The extension of the TISs spans the whole trivial Sb_2Te_3 subsystem. All the topological states shown are degenerate due to inversion symmetry, and only one of the twofold degenerate states is shown in each case (with the other state always being localized at the opposite surface or interface).

other hand, the 6 QL Bi_2Te_3 slab under purely biaxial strain is a TI which develops TSSs with no gap, and its DP lies below the Fermi level—Fig. 9(a). When the two subsystems are brought together, the bulk-to-boundary correspondence dictates that topologically protected interface states must develop in the gap. The band structures of the junctions are shown in Figs. 13(a) to 13(f).

For periodic boundary conditions—panels (a) to (c) of Fig. 13—and in contrast to the TI/TI superlattices analyzed in Sec. IV A, a topological interface state (TIS) develops that spans the bulk band gap. Unexpectedly, the interface

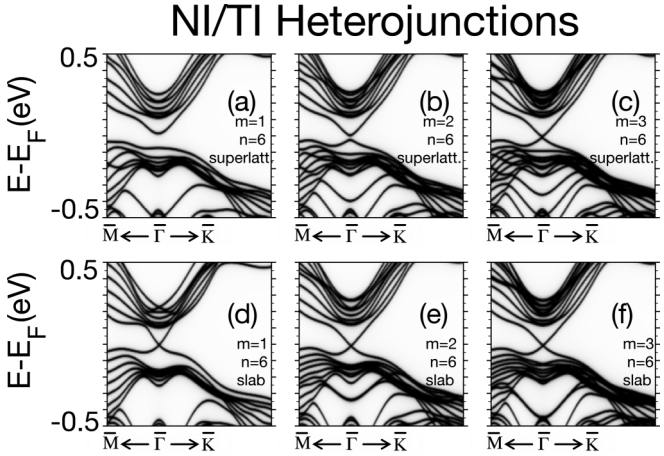

FIG. 13. Band structure of the NI/TI/NI heterojunctions considered, both in superlattice—(a) to (c)—and slab—(d) to (f)—geometries. Panels (a), (b), and (c) show the band dispersion for the superlattices with $n = 6$ and $m = 1$, 2, and 3, respectively. As the Sb_2Te_3 subsystem has been driven to the normal insulating phase by applying uniaxial tensile tension, topologically protected states localized at the interface appear, according to the bulk-to-boundary correspondence. A gap in the spectrum opens for m below $\sim$2 due to interface-interface interaction (note that the total thickness of the Sb_2Te_3 subsystem is $2m$ QLs in the superlattices). Panels (d), (e), and (f) correspond to slab geometries with $n = 6$ and $m = 1$, 2, and 3, respectively. In these three cases a topological interface state (TIS) develops irrespective of the number of Sb_2Te_3 layers.

topological state localizes in the normal insulator Sb_2Te_3 (see Fig. 14), as opposed to TSSs, which always localize in the topological insulator. In this heterojunction a hybridization gap opens in the spectrum for thicknesses of the $2m-Sb_2Te_3$ layer below $m = 2$ QLs—Fig. 13(b)—since the two opposed interfaces are closer than twice the penetration depth of the TISs. The TISs show no doping in contrast with the TSS of 6 QL Bi_2Te_3—see Fig. 13(f), opening a new way of tuning the DP energy of the topological states.

To understand the fundamental difference between the TI/TI and NI/TI heterojunctions, we analyze the atomic orbital PDOS at $\bar{\Gamma}$ in Figs. 11 and 15. While the Bi_2Te_3 shows band inversion in both cases, the Sb_2Te_3 subsystem exhibits opposite traits in the two different sets of heterojunctions. In the TI/TI systems, as discussed previously, there is band inversion, while in the NI/TI there is not. In the NI/TI case the Te p_z orbital of the Sb_2Te_3 with negative parity occupies the top of the VB region, while the Sb p_z orbital with positive parity is located at the CB just above the Te derived bands of Bi_2Te_3. Therefore, the Sb_2Te_3 remains in the trivial state. Nevertheless, the topological interface states are mainly formed from the orbitals closest to the energy gap, namely from the Te orbitals of Sb_2Te_3. This feature explains why the TISs are located predominantly in the nontopological slab. Furthermore, due to their spatial localization, there is a strong interaction between the TISs at both interfaces for $m = 1$ and 2, and a gap opens up.

For the trilayer slab configurations shown in panels (d) to (f) of Fig. 13, the system shows a common bulk gap of $\sim$0.15 eV and a gapless interface state with the DP at the Fermi level. This topological interface state is also undoped and

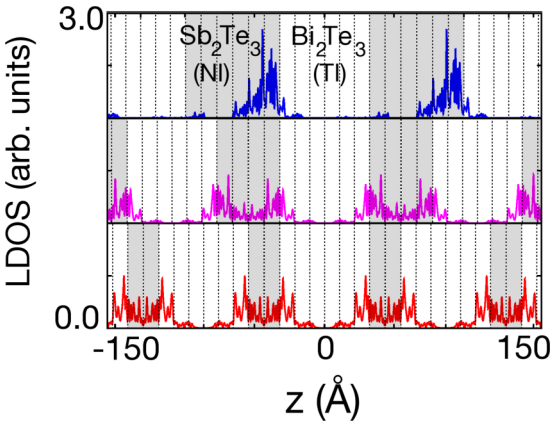

FIG. 14. LDOS of the TISs in $m-Sb_2Te_3/n-Bi_2Te_3/m-Sb_2Te_3$ superlattices for $m = 1$ (red line at the bottom), $m = 2$ (magenta line in the middle), and $m = 3$ (blue line at the top)—note that the total thickness of the Sb_2Te_3 subsystem is $2m$ QLs. The LDOS was computed at $\boldsymbol{k} = (5,0) \times 10^{-3}$ Å^{-1}, along the $\bar{\Gamma} - \bar{K}$ direction and close to the $\bar{\Gamma}$ point for the electronlike TISs. The system is centered at the middle of the 6 QL Bi_2Te_3 layer. Vertical dashed lines depict the boundaries of each QL. The gray shaded region corresponds to the Sb_2Te_3 subsystem, while white regions belong to the Bi_2Te_3 subsystem. TISs of NI/TI superlattices exhibit strong hybridization with the opposite interface for thicknesses of the $2m-Sb_2Te_3$ layer below $m = 2$ QLs, while for the $m = 3$ QLs the TISs are already decoupled. All three TISs shown are degenerate due to inversion symmetry, and only one of the twofold degenerate states is shown in each case.

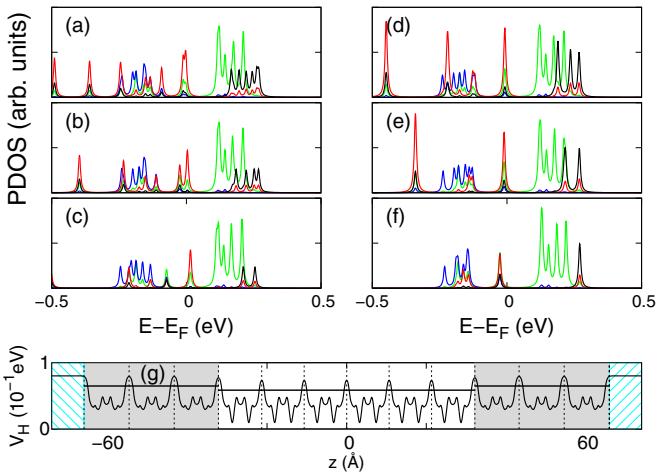

FIG. 15. Panels (a) to (f) show the PDOS in $\bar{\Gamma}$ close to the Fermi level of the studied NI/TI heterojunctions. Blue and black lines show the contribution of Bi p_z and Sb p_z orbitals, respectively. The green and red lines indicate the Te p_z contributions from the Te atoms in the Bi_2Te_3 and Sb_2Te_3 subsystems, respectively. Panels (a) to (c)—(d) to (f)—depict the PDOS for superlattices—slabs—with $m = 3$ to 1. The Bi_2Te_3 subsystem shows band inversion, while the Sb_2Te_3 subsystem is uninverted. The 2D averaged Hartree potential profile for the $m = 3$ NI/TI slab is shown in (g), along with the average Hartree potential in each QL (horizontal straight solid lines).

develops irrespective of the thickness of the nontopological Sb_2Te_3 layers and, analogous to the emergent TISs in the SLs, it is not strictly localized at the interface. Instead, the state at the gap is confined in the Sb_2Te_3 subsystem, with more weight at the interfacemost QL of Sb_2Te_3, but exceeding the expected ∼2 QL penetration depth of the TSSs in an isolated Bi_2Te_3 slab—see Fig. 12(b). Moreover, the orbital distribution in the VB and CB, and hence that of the TIS, is similar in the NI/TI superlattices and trilayers (see Fig. 15). The main difference between the superlattice and the trilayer TISs lies in the lack of interaction in the trilayer geometry due to the localization in the Sb_2Te_3 subsystem. Thus all the trilayers remain semimetallic. On the other hand, only minor differences between the averaged Hartree potential of NI/TI and TI/TI heterostructures of equivalent TI/TI geometry—see Fig. 11(g) and Fig. 15—are observed.

Our findings are in agreement with previous results [38–41] in which similar TISs with large penetration depths appear in NI/TI junctions localized in the NI. We additionally checked that in NI/TI/NI heterojunctions of $m-Sb_2Te_3/n-Bi_2Te_3/m-Sb_2Te_3$ with n as low as 1 QL, the TISs are always gapless in slab configuration, and remain gapless in superlattice geometries as long as $m > 2$. Note that Bi_2Te_3 here is the TI, and 1 QL Bi_2Te_3 thin films show a relatively large Dirac gap due to surface-surface hybridization. Therefore, capping Bi_2Te_3 with uniaxially strained Sb_2Te_3 leads to a closing of the Dirac gap in the topological states, since the latter localizes in the normal insulating Sb_2Te_3. In addition, although the development of TISs in NI/TI junctions is dictated by topology, their spatial location is determined by the orbitals dominating the edges of the valence and conduction band of the heterostructures, and thus by the relative alignment of the bands of both subsystems.

V. SUMMARY AND CONCLUSIONS

We have shown the combined effects of uniaxial and biaxial strain on Bi_2Te_3, Sb_2Te_3, Bi_2Se_3, and Sb_2Se_3, both in bulk and slab geometries. A phase diagram for the four systems was computed and analyzed, demonstrating that topological phase transitions, either to a metal or to a trivial insulator, can occur for different combinations of both kinds of strains, and a universal behavior was found for the four compounds. We showed how strain can engineer the DP energy, the Fermi velocity, the metallic character, and the topology of the four compounds, thus offering a wide tunability regarding straintronics. We have also calculated the electronic structure of $Sb_2Te_3/Bi_2Te_3/Sb_2Te_3$ trilayers, in which Sb_2Te_3 was driven into the topologically trivial insulating regime by applying uniaxial strain. For the TI/TI systems no trivial nor topological interface state is found, and the superlattice shows a straddling gap of ∼0.1 eV. In the NI/TI heterojunctions, topologically protected interface states are predicted and characterized. Since the TIS spatial location is determined by the relative band alignment of the two compounds forming the heterostructures, we find TISs to localize in the NI both in slab configurations and periodic superlattices, thus opening a route to closing hybridization gaps in topological states of ultrathin films of the Bi_2Se_3 family by capping the system with NI layers. Our results for the NI/TI heterojunctions also indicate a way to avoid interactions of the topological states with undesired ambient impurities while preserving the bulk band gap of the system, and thus maintaining the topological protection

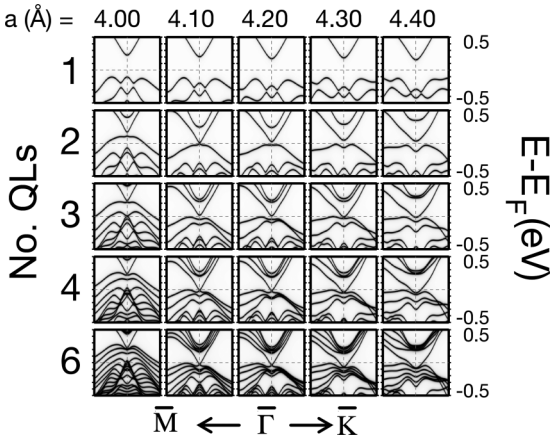

FIG. 16. Same as Fig. 7 for Bi_2Te_3.

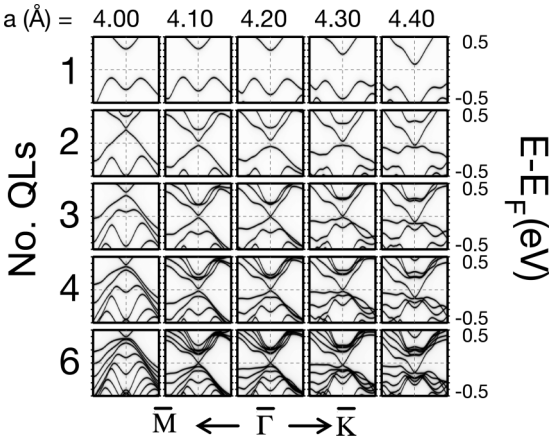

FIG. 17. Same as Fig. 7 for Sb_2Te_3.

of the states. Uniaxial strain on the Sb_2Te_3 subsystem can additionally turn the interface conducting channel on or off; thus the system hosts a switchable topological interface state irrespective of the thickness of the TI layer.

ACKNOWLEDGMENTS

This work has been supported by the Spanish Ministry of Economy and Competitiveness through Grant MINECO/FEDER No. MAT2015-66888-C3-1R. We acknowledge the use of computational resources of CESGA, Red Española de Supercomputación (RES), and the i2BASQUE academic network.

APPENDIX: BAND DISPERSION TABLES FOR Bi_2Te_3, Sb_2Te_3, AND Sb_2Se_3

Figures 16, 17, and 18 contain band dispersion diagrams for Bi_2Te_3, Sb_2Te_3, and Sb_2Se_3, respectively.

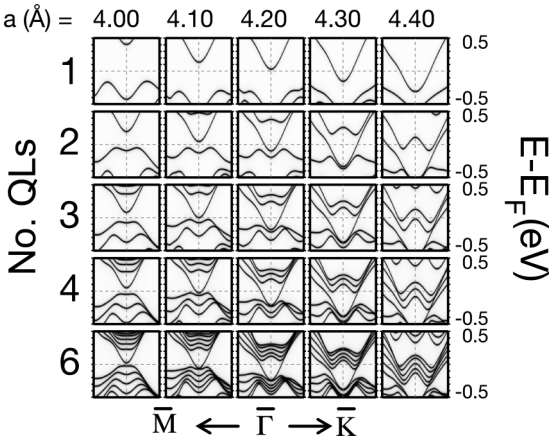

FIG. 18. Same as Fig. 7 for Sb_2Se_3.

[1] L. Fu, C. L. Kane, and E. J. Mele, Phys. Rev. Lett. **98**, 106803 (2007).
[2] R. Roy, Phys. Rev. B **79**, 195322 (2009).
[3] C. L. Kane and E. J. Mele, Phys. Rev. Lett. **95**, 146802 (2005).
[4] M. Z. Hasan and C. L. Kane, Rev. Mod. Phys. **82**, 3045 (2010).
[5] H. Zhang, C.-X. Liu, X.-L. Qi, X. Dai, Z. Fang, and S.-C. Zhang, Nat. Phys. **5**, 438 (2009).
[6] S. Basak, H. Lin, L. A. Wray, S.-Y. Xu, L. Fu, M. Z. Hasan, and A. Bansil, Phys. Rev. B **84**, 121401 (2011).
[7] H. Aramberri, J. I. Cerdá, and M. C. Muñoz, Nano Lett. **15**, 3840 (2015).
[8] Y. Liu, Y. Y. Li, S. Rajput, D. Gilks, L. Lari, P. L. Galindo, M. Weinert, V. K. Lazarov, and L. Li, Nat. Phys. **10**, 294 (2014).
[9] S. M. Young, S. Chowdhury, E. J. Walter, E. J. Mele, C. L. Kane, and A. M. Rappe, Phys. Rev. B **84**, 085106 (2011).
[10] X. Luo, M. B. Sullivan, and S. Y. Quek, Phys. Rev. B **86**, 184111 (2012).
[11] Y. V. Lysogorskiy, A. G. Kijamov, O. V. Nedopekin, and D. A. Tayurskii, J. Phys.: Conf. Ser. **394**, 012022 (2012).
[12] J. Liu, Y. Xu, J. Wu, B.-L. Gu, S. B. Zhang, and W. Duan, Acta Crystallogr. Sect. C **70**, 118 (2014).
[13] W. Liu, X. Peng, C. Tang, L. Sun, K. Zhang, and J. Zhong, Phys. Rev. B **84**, 245105 (2011).
[14] L. Zhao, J. Liu, P. Tang, and W. Duan, Appl. Phys. Lett. **100**, 131602 (2012).
[15] K. J. Koski, C. D. Wessells, B. W. Reed, J. J. Cha, D. Kong, and Y. Cui, J. Am. Chem. Soc. **134**, 13773 (2012).
[16] T.-H. Kim, K. Jeong, B. C. Park, H. Choi, S. H. Park, S. Jung, J. Park, K.-H. Jeong, J. W. Kim, J. H. Kim, and M.-H. Cho, Nanoscale **8**, 741 (2016).
[17] G. Kresse and J. Hafner, Phys. Rev. B **48**, 13115 (1993).
[18] J. M. Soler, E. Artacho, J. D. Gale, A. García, J. Junquera, P. Ordejón, and D. Sánchez-Portal, J. Phys.: Condens. Matter **14**, 2745 (2002).
[19] J. I. Cerdá, M. A. Van Hove, P. Sautet, and M. Salmeron, Phys. Rev. B **56**, 15885 (1997).
[20] J. P. Perdew, K. Burke, and M. Ernzerhof, Phys. Rev. Lett. **77**, 3865 (1996).

[21] S. Grimme, J. Comput. Chem. **27**, 1787 (2006).
[22] Y.-S. Kim, K. Hummer, and G. Kresse, Phys. Rev. B **80**, 035203 (2009).
[23] R. Cuadrado and J. I. Cerdá, J. Phys.: Condens. Matter **24**, 086005 (2012).
[24] M. Ohring, *Materials Science of Thin Films* (Academic, New York, 2001).
[25] R. W. G. Wyckoff, *Crystal Structures* (Wiley, New York, 1964).
[26] X. Gao, M. Zhou, Y. Cheng, and G. Ji, Philos. Mag. **96**, 208 (2016).
[27] H. Koc, A. M. Mamedov, and E. Ozbay, *Applications of Ferroelectric and Workshop on the Piezoresponse Force Microscopy (ISAF/PFM), 2013 IEEE International Symposium* (IEEE, New York, 2013), pp. 41–44.
[28] O. V. Yazyev, E. Kioupakis, J. E. Moore, and S. G. Louie, Phys. Rev. B **85**, 161101 (2012).
[29] I. Aguilera, C. Friedrich, G. Bihlmayer, and S. Blügel, Phys. Rev. B **88**, 045206 (2013).
[30] B. Monserrat and D. Vanderbilt, Phys. Rev. Lett. **117**, 226801 (2016).
[31] J. Black, E. M. Conwell, L. Seigle, and C. W. Spencer, J. Phys. Chem. Solids **2**, 240 (1957).
[32] W. Li, X.-Y. Wei, J.-X. Zhu, C. S. Ting, and Y. Chen, Phys. Rev. B **89**, 035101 (2014).
[33] B. Ryu, B.-S. Kim, J. E. Lee, S.-J. Joo, B.-K. Min, H. Lee, S. Park, and M.-W. Oh, J. Korean Phys. Soc. **68**, 115 (2016).
[34] I. Efthimiopoulos, J. Zhang, M. Kucway, C. Park, R. C. Ewing, and Y. Wang, Sci. Rep. **3**, 2665 (2013).
[35] G. H. Cao, H. J. Liu, J. H. Liang, L. Cheng, D. D. Fan, and Z. Y. Zhang, arXiv:1607.05911 [cond-mat].
[36] L. Pauling, J. Am. Chem. Soc. **54**, 3570 (1932).
[37] L. C. Allen, J. Am. Chem. Soc. **111**, 9003 (1989).
[38] Q. Zhang, Z. Zhang, Z. Zhu, U. Schwingenschlögl, and Y. Cui, ACS Nano **6**, 2345 (2012).
[39] V. N. Men'shov, V. V. Tugushev, T. V. Menshchikova, S. V. Eremeev, P. M. Echenique, and E. V. Chulkov, J. Phys.: Condens. Matter **26**, 485003 (2014).
[40] M. J. Brahlek, N. Koirala, J. Liu, T. I. Yusufaly, M. Salehi, M.-G. Han, Y. Zhu, D. Vanderbilt, and S. Oh, Phys. Rev. B **93**, 125416 (2016).
[41] T. V. Menshchikova, M. M. Otrokov, S. S. Tsirkin, D. A. Samorokov, V. V. Bebneva, A. Ernst, V. M. Kuznetsov, and E. V. Chulkov, Nano Lett. **13**, 6064 (2013).